

pubs.acs.org/est Article

# Rare Earths Recovery from Calcium-Rich Coal Fly Ash: Secondary Phase Formation and Mitigation Approaches

Published as part of Environmental Science & Technology special issue "Advancing a Circular Economy". Sheila Gerardo and Wen Song\*



Cite This: Environ. Sci. Technol. 2025, 59, 23592-23601



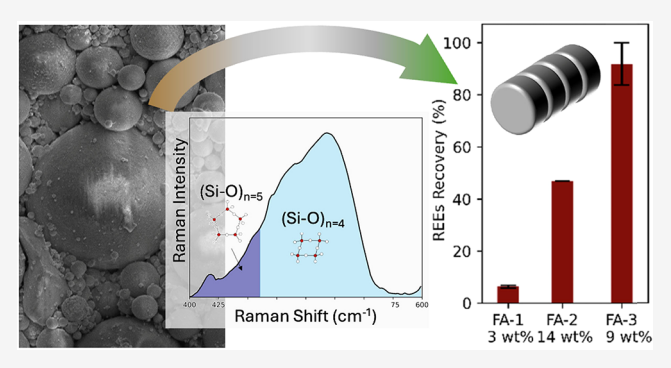
**ACCESS** I

III Metrics & More

Article Recommendations

Supporting Information

**ABSTRACT:** Rare earth elements (REEs) extraction from legacy coal ash enables simultaneous waste valorization and remediation. Ashes enriched in basic compounds (e.g., CaO) lend particularly well to REEs extraction but are prone to precipitate formation that hinders upscaled implementation. This study characterizes the secondary phase precipitation that occurs during mild acid leaching and develops an approach to circumvent their formation while maintaining effective REEs recovery. Notably, precipitate characteristics vary with leachant acidity: very acidic solutions (pH < 0) condense silica gels but achieve  $\sim 90$  % REEs recovery, whereas mild pH values ( $\sim 3.5$ ) precipitate aluminosilicate flocs and are limited to low REEs recoverability ( $\sim 30$  to 55 %). Gel precipitates,



however, alter the rheology of the leachate via their transformation to a semicondensed phase, and are problematic in upscaled operations. To minimize gel formation, we evaluate alternative extraction methods, including an acid baking (i.e., dry digestion) approach that circumvents secondary precipitates while yielding high REEs extractability of  $\sim 74$  % and low co-extraction of secondary elements. Together, the results here provide key insights critical to controlling acid leaching of ash feedstocks and provide alternative methods for REEs extraction that bypass gel and floc precipitation to enable effective REEs recovery from coal ash wastes.

KEYWORDS: rare earth elements, REEs, precipitation, gel, acid baking, dry digestion

# **■** INTRODUCTION

Rare earth elements (REEs), comprised of the lanthanide series along with Sc and Y, hold unique magnetic and catalytic properties critical across modern technologies. <sup>1–5</sup> Increased use of electronics, sustainable energy, defense, and medical infrastructure is projected to raise REEs demand three- to 7-fold by 2040. Satisfying this rapid demand will require alternative unconventional REEs resources. Coal fly ash, an abundant legacy waste generated in coal-fired power plants, contains up to ~ 1500 ppm of REEs and presents an exciting opportunity as an abundant and ubiquitous resource. <sup>7,8</sup> In the United States alone, fly ash could yield ~12 000 tons of REEs annually, surpassing current U.S. consumption. <sup>9–11</sup> Extracting REEs from fly ash repositories, many of which are piled in unlined landfills, provides an exciting opportunity to simultaneously remediate and valorize toxic environmental wastes.

The efficacy of REEs extraction, however, hinges on the elemental and mineralogic composition of the ash feed-stock. <sup>12,13</sup> In coal fly ash, discrete REE-bearing minerals (e.g., phosphates, oxides, fluorocarbonates, etc., that incorporate the rare earth elements into their lattice structure) <sup>14,15</sup> exist in one of three modes: ~80% encapsulated in dense amorphous ash

particles without internal porosity or pore connectivity necessary for interfacial reaction and reagent transport,  $\sim \! 10\%$  encapsulated in porous ash particles, and the remainder as discrete free-floating REE minerals or bound to the surface of an ash particle accessible directly to reagents. While the latter two are amenable to interfacial REE mineral dissolution reactions, the effective extraction of REEs must unlock pathways for REE mineral dissolution from dense amorphous ash matrices.

Recent advances show that effective REEs extraction from dense amorphous ash particulates is possible, where glassy matrices bearing high concentrations of alkali and alkali-earth metals enable solid-state intermolecular diffusion and metaloxide hydrolysis without bulk dissolution. <sup>12,13,16</sup> Specifically, loosely held metal cations (e.g., Ca, Al, Fe, etc.) in the glassy matrix are released readily upon exposure to protons (i.e.,

Received: June 30, 2025 Revised: September 6, 2025 Accepted: September 10, 2025 Published: September 16, 2025





cation exchange). The liberated metal cations diffuse outward through the vacated molecular interstices while protons diffuse into the glassy ash matrix for further exchange reactions. Notably, ashes rich in calcium (i.e., class C ash, CaO wt > 18%) are particularly amenable to this solid-state reaction-diffusion process, where milder and less reagent-intensive approaches (e.g., nitric acid, hydrochloric acid, etc.) have achieved ~70–100% recovery of the total REEs available in the ash. P18–20 By contrast, Ca-poor ashes (class F ash, CaO wt < 18%) vielded ~10–40% recovery using the same approach. S18–20 Ca-rich ashes, therefore, are particularly attractive for REEs extraction due to their high REEs extractability and minimal reagent requirements.

REEs leaching from Ca-rich ash, however, is coupled frequently with secondary precipitates.  $^{16,18}$  Under both mild pH values (e.g., pH  $\sim$  4) and strongly acidic cases (pH < 0), secondary phases (e.g., particles, gels, etc.) precipitate readily, which undermines industrial operations.  $^{16,18}$  The drawbacks of secondary phase formations in hydrometallurgical operations, including the acidic leaching of REEs from coal ash, are understood from the point of view of upscaled operations and downstream processing. Specifically, precipitates increase the viscosity of the REE-impregnated leachate, reduce solution filterability, and ultimately limit the economic feasibility of upscaled hydrometallurgical operations.  $^{21}$  To inform industrial practice, the impact of secondary phases on REEs recovery from coal fly ash and approaches to circumvent their formation — so far elusive — must be elucidated.

In this study, we (i) characterize the secondary phases formed during acid leaching of calcium-rich coal fly ash, (ii) determine the impact of precipitation on REEs recovery, and (iii) develop approaches to minimize precipitation while maintaining economic rates of REEs extraction. Precipitate formation was probed using nitric acid (HNO<sub>3</sub>, 1-6 M), in keeping with the high REEs recoveries demonstrated previously in nitric environments, and liquid-solid ratios of 10 that result in favorable leaching efficacies for a range of acidic media. 16,18 The physicochemical properties of the reaction products were probed using scanning electron microscopy (SEM-EDS), X-ray diffraction (XRD), and Raman spectroscopy. Product formation was corroborated by fluid chemical analyses and thermodynamic calculations. Leaching with 6 M HNO<sub>3</sub> produced a silica-rich gelatinous phase, while a 1 M HNO<sub>3</sub> solution precipitated aluminosilicate-rich flocculants. Potential transport-limiting effects induced by gelation were evaluated using solute transport experiments, and the overall impact of precipitates on REEs recovery was investigated using time-resolved fluid analysis. Lastly, we investigate three REE extraction approaches that circumvent secondary phase formation while achieving high REE recovery efficiencies: greater liquid-solid ratios, intermediate acid concentration leaching, and a novel acid baking method. Our results show that acid baking holds promise for REEs extraction from fly ash and yields high extraction efficiencies with low dissolved concentrations of major cations when compared to state-of-the-art direct leaching. We note that although acid baking has been used in monazite ore processing, 22 only recently has this method been tested in unconventional REE resources, 23-26 and, to the best of our knowledge, this is the first report of its application to circumvent gelation during REEs extraction from coal fly ash. The findings reported here advance our understanding of key processes governing REEs extraction from ash to enable the

development of economically feasible and environmentally benign approaches to simultaneously valorize and remediate ash wastes.

## MATERIALS AND METHODS

Coal Fly Ash Samples. Four coal fly ash samples with varying calcium concentrations were used in this study. Ash aliquots were sieved using a no. 60 mesh (250  $\mu$ m diameter) to remove clastic contaminants and stored in closed containers. We note here that the mesh size is substantially larger than the ash particles (<100  $\mu$ m) to separate rock fragments without discarding the target ash phase. To characterize the elemental composition of each ash sample, full acid digestion was carried out using a HF-HNO3 microwave-assisted procedure. Specifically,  $\sim 25$  mg of ash was loaded into PTFE vials along with 3 mL of Optima hydrofluoric acid and 1 mL of concentrated nitric acid. The ash aliquots were digested for 1 h at 280 °C and 115 bar using a microwave digestion system (Anton-Parr Multiwave 7000). The resulting effluents were transferred to clean PFA vials, dried down, and redigested using 3 mL of aqua regia to ensure a solid-free digested effluent. The final effluents were dried down, redissolved using dilute nitric acid, and their elemental compositions were determined using a quadrupole inductively coupled plasma mass spectrometry (ICP-MS, Agilent 7500ce). Total REEs concentrations in the ashes range from 313 to 622 ppm, with calcium concentrations (reported as oxide equivalent) of 2.6-27.9 wt. % and iron contents (reported as oxide equivalent) typically ~ 5 wt. % (Tables S1 and S2). Sample FA-1 was an exception, where iron oxide was 20.7 wt. % (Table S1).

Bulk phase composition was determined using a powder X-ray diffractometer (XRD, Rigaku Miniflex 600 Diffractometer) with a Cu K $\alpha$  radiation source operated at a voltage of 40 kV, current of 15 mA, and a scan speed of 1°/min. Major phases present in the ash samples included an amorphous aluminosilicate phase, quartz (SiO<sub>2</sub>), mullite (3Al<sub>2</sub>O<sub>3</sub>·2SiO<sub>2</sub>), anhydrite (CaSO<sub>4</sub>), periclase (MgO), lime (CaO), calcium silicate (CaSiO<sub>3</sub>), hematite ( $\alpha$ -Fe<sub>2</sub>O<sub>3</sub>), and maghemite ( $\gamma$ -Fe<sub>2</sub>O<sub>3</sub>) (Figure S1).

Bulk Leaching Experiments and Solids Separation. Leaching experiments were performed using nitric acid solutions with molarities ranging from 1 to 6 M. First, 2.5 mL of acid solution was transferred to Savillex perfluoroalkoxy (PFA) vials and preheated for 45 min at 80 °C using a hot plate equipped with a heating block and temperature control. Fly ash aliquots were then added to the preheated solution, mixed, and reacted for up to 4 h to elucidate the kinetics of the acid leaching reaction with ash samples. Previous research shows that 4 h is sufficient time to reach reaction equilibrium here.

The final leachates were transferred into clean polypropylene (PPE) tubes and, when possible, decanted into separate vials to differentiate the portion hosting the residual ash from the portion hosting the secondary precipitate phases. Specifically, physical separation via decantation was performed to isolate the newly formed phases from the residual ash particulates. This approach separates the ash residues from the precipitates by leveraging their differential densities. Here, the newly formed phases suspended in the leachate are decanted into a new PPE tube, while the heavier residual ash is retained in the original vessel. Leachates were then centrifuged and filtered using a 0.45  $\mu m$  PTFE syringe filter to remove any particulates, and the resulting effluents were transferred into clean PPE

tubes for further analysis. The remaining solid materials were triple-washed using deionized (DI) water, air-dried for  $\sim$ 3 days, and reserved for further characterization. Leaching experiments were performed in quadruplicate, where the resulting effluents of two runs were diluted immediately and reserved for ICP-MS elemental analysis, and the resulting effluents of the remaining runs were used for pH measurements. Liquid—solid ratios of 10 (weight/weight basis) were used for the leaching experiments, unless noted otherwise. Trace metal grade nitric acid (HNO3, Fisher Scientific) was used in all leaching experiments.

To better understand the precipitation behavior of different leachates, thermodynamic calculations were performed by using PHREEQC, an open-source geochemical modeling tool, along with the Minteq thermodynamic database. Additional solubility products of mineral phases of interest (i.e., REEs hydroxides) were compiled <sup>27–29</sup> and added to the database to evaluate potential REEs losses through precipitation. The input files for the calculations consisted of the leachate pH measurements along with the measured concentrations of major cations and REEs in solution. Nitrate (NO<sub>3</sub><sup>-</sup>) concentration was also included based on the molarity of the initial acid solution used. As an output, PHREEQC provides the aqueous speciation data and calculated saturation indices (SI). The output saturation indices were used to evaluate whether the precipitation of a particular mineral is likely to occur. Specifically, a positive saturation index (SI > 0) indicates that the solution is oversaturated with respect to a mineral and, thus, precipitation is favorable, while a negative saturation index (SI < 0) indicates that the solution is undersaturated and, therefore, species will remain in the aqueous solution (i.e., precipitation will not occur).

Precipitate and Secondary Phase Characterization. The physicochemical properties of the precipitated phases were evaluated by using scanning electron microscopy (SEM-EDS), XRD, micro-Raman spectroscopy, and solute transport experiments.

First, phase and elemental characterization of the precipitates formed during acid leaching were carried out using XRD and SEM-EDS (Scios 2HiVac), respectively. The dried precipitates were homogenized using a mortar and pestle prior to analysis. XRD samples were loaded in a zero-background silicon holder and analyzed using a voltage of 40 kV, current of 15 mA, and scan speed of 1.5°/min. For microscopic characterization, the precipitates were mounted on an aluminum stub using double-sided carbon tape and lightly sputtered (<10 s, Au–Pd EMS Sputter coater) to minimize charge accumulation and to improve EDS data collection.

Second, the chemical properties of secondary phases were further evaluated in their original hydrated state by using micro-Raman spectroscopy. Specifically, gelled leachates were characterized using an optical microscope (Nikon Eclipse Lvidia-N) equipped with a Raman spectrometer (Horiba i320) and a 532 nm laser source. The resulting spectrum was corrected for baseline shifts and normalized using the water band peak at 1645 cm<sup>-1</sup> (OH bending vibration mode) as the internal standard. While characteristic broad band peaks for amorphous phases of interest lie in the 250–600 cm<sup>-1</sup> wavenumber range, our analysis focused primarily in the 400–600 cm<sup>-1</sup> region since Rayleigh scattering interference impedes the analysis of lower wavenumber spectral bands. Relevant band peaks used in this study include those in the

400–460 cm<sup>-1</sup> region, indicative of 5-fold or larger Si–O–Si rings, and the band at 488–495 cm<sup>-1</sup> characteristic of 4-membered Si–O–Si rings.<sup>32</sup> The degree of polymerization of the precipitate was qualitatively assessed using an integrated intensity ratio,  $R_{\rm n}$ ,  $^{31,32}$  defined as the ratio of the integrated intensity of the five-membered ring peak to the integrated intensity of the entire amorphous broad band ( $R_{\rm n} = \int_{400}^{460} I d\tilde{v} / \int_{400}^{600} I d\tilde{v}$ ).

Third, to determine the transport properties of the gels, solute transport studies were performed using copper nitrate (CuNO<sub>3</sub>, Sigma-Aldrich). Copper was selected as the solute for its distinctive color in solutions, which enables visual tracking of the solute front position and direct colorimetric concentration measurement. Gel columns were prepared by mixing FA-3 with 6 M HNO<sub>3</sub> at a liquid—solid ratio of 10 (weight/weight basis). The acid-ash mixture was prepared in a 50 mL PPE test tube in the upright position to ensure that the ash settled at the bottom, while the leachate remained at the top of the column. The leachate was allowed to gel overnight at room temperature. Approximately 3 mL of a 0.5 M CuNO<sub>3</sub> solution was then placed on top of the gel and allowed to diffuse through the gel phase.

Following the CuNO<sub>3</sub> diffusion (e.g., after 24 and 52 h), the gel phase was sectioned along its length to evaluate the impact of gel on cation (i.e., Cu<sup>2+</sup>) transport. Each gel section was centrifuged, and the concentration of the fluids entrained in the gel was measured using an Agilent Cary 60 UV—vis Spectrometer at 800 nm. The data were cast on a calibration curve generated using standard Cu<sup>2+</sup> solutions with concentrations that range between 0.005 and 0.075 M (Figure S2). The absorbance of the initial leachate was also obtained to subtract background signals. Lastly, spatiotemporal concentration profiles were used to model the diffusion of Cu<sup>2+</sup> cations across the gelled phase. For simplicity, the system was modeled as a 1D unsteady diffusion process (eq 1)

$$\frac{\partial C}{\partial t} = D \frac{\partial^2 C}{\partial x^2} \tag{1}$$

where C is the solute concentration, x is the position along the gel column, t is the time, and D is the diffusion coefficient. We assume a thin source of solute in a semi-infinite medium  $(C(x \to \infty, t) = 0)$ , constrained by the mass conservation of the solute  $(\int C(x, t) \, \mathrm{d}x = N)$ , where N is the amount of solute in the system), and zero concentration in the gel at initial time C(x, t = 0) = 0. The analytical solution (eq 2) was used to determine the diffusion coefficient, enabling a first-order approximation of the diffusive properties of cations across the gelled leachate.

$$C(x, t) = \frac{N}{\sqrt{\pi Dt}} e^{-x^2/4Dt}$$
(2)

Acid Baking Experiments. Acid baking experiments were performed using the FA-3 ash sample. First, ~200 mg of the ash sample was transferred into PFA vials, and 800 mg of 15 M nitric acid was added to the vial (acid—solid ratio of 4:1, weight/weight basis). The mixture was dried down at 120 °C for 2 h using a hot plate equipped with a heating block and temperature control. Following digestion, the resulting solids were ground using a mortar and pestle, transferred into clean vials, and 2 mL of DI water was added for postbaking leaching. The water leaching step proceeded for 6 h at room temperature. Samples were agitated periodically during

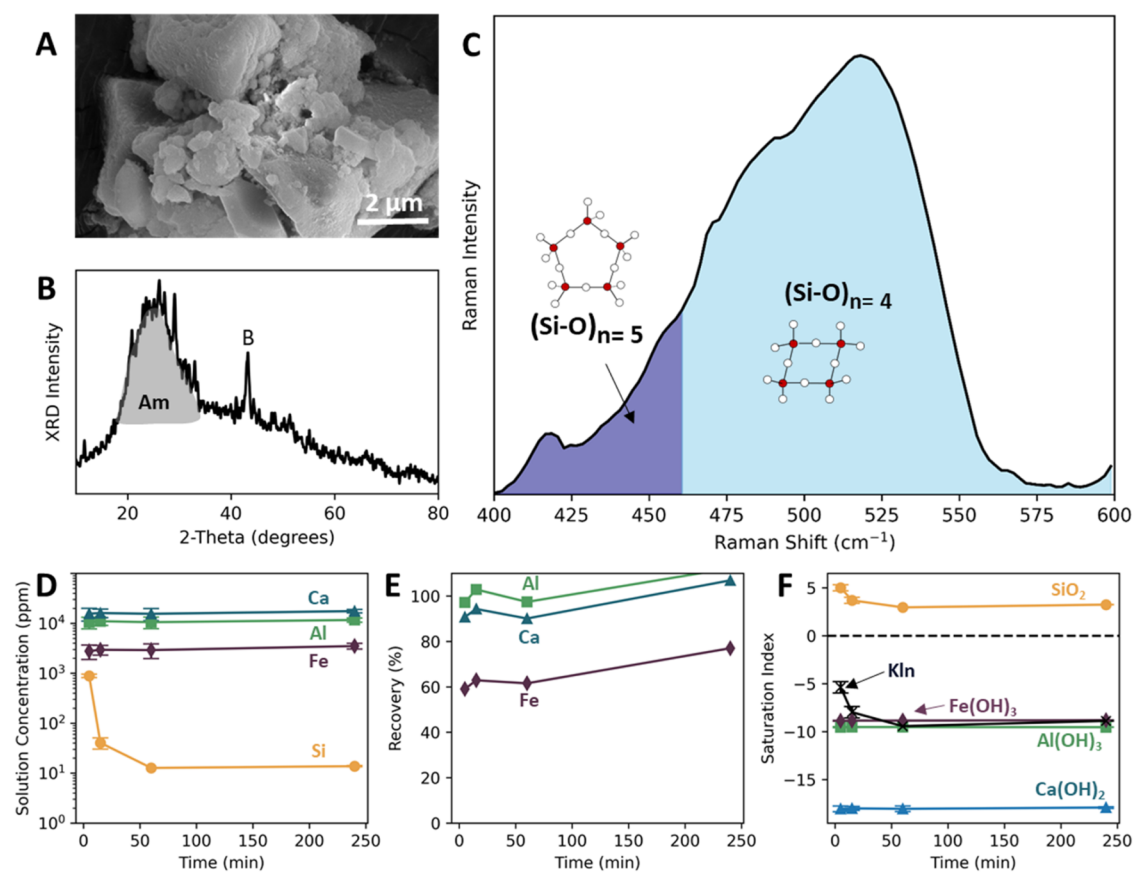


Figure 1. Characterization of gels precipitated during 6 M HNO<sub>3</sub> leaching of the FA-3 ash sample. (A) Microscopic characterization of the dried gels collected by using SEM (B) XRD spectra of the dried gel. The shaded region denoted as "Am" corresponds to the amorphous phase, and the peak denoted as B corresponds to Barite that likely originated from insufficient precipitate wash. (C) Raman spectra of gels in their native hydrated state. The region corresponding to five-membered silica rings is shaded in light blue. Molecular representations have been added depicting the approximate structure of the silica rings, where white circles represent oxygen and red circles represent silicon. (D) Concentration measurements, in ppm, of Si, Ca, Al, and Fe in solution. Si concentrations decrease by 2 orders of magnitude from 5 to 240 min, indicating precipitation of Si-rich phases. (E) Recovery efficiencies of major cations in solution. (F) Calculated saturation indices for key mineral phases, including amorphous silica (SiO<sub>2(a)</sub>), kaolinite, goethite, gibbsite, and portlandite. The positive saturation index of amorphous silica indicates that the solution is oversaturated and precipitation of this phase is thermodynamically favorable.

leaching using a Vortex mixer at 1200 rpm (30 s pulses each hour). The resulting leachates were centrifuged to separate the remaining solid phases, further diluted using 2% HNO<sub>3</sub>, and analyzed for their elemental composition using ICP-MS.

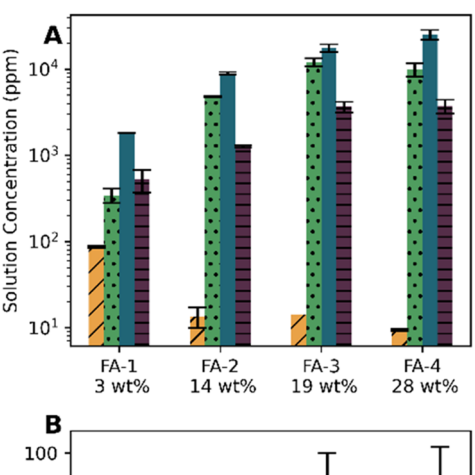
# ■ RESULTS AND DISCUSSION

Secondary Phases in Highly Acidic Solutions (pH < **0).** Precipitate Characteristics. Ash leaching using a 6 M HNO<sub>3</sub> solution precipitated a gelatinous phase (Figure 1). Semiquantitative elemental characterization using SEM-EDS shows that the gel structural framework is composed primarily of silica (~36 wt. % Si and ~43 wt. % O, Figures 1A and S3). Minor elements include Al, Ca, and P. XRD analysis of the dehydrated gel shows an amorphous hump<sup>33</sup> and, along with the elemental data collected, indicates that the precipitates in the gel consist primarily of amorphous silica (Figure 1B). Raman spectroscopy of the native hydrated gel further corroborates the in situ composition of the precipitated phase, with broad Raman band peaks in the 400-600 cm<sup>-1</sup> characteristic of amorphous silica (Figure 1C). The calculated Raman integrated intensity ratio was  $R_{\rm n} \sim 0.22$ , suggesting a higher prevalence of four-membered silica rings that are

polymerized into nanometer-sized nuclei ( $\sim$ 2–4 nm). <sup>34</sup> These molecular nuclei further condense into three-dimensional chain-like structures that trap water through capillary effects and produce a hydrated gel. <sup>34,35</sup>

Elemental characterization of the fluid entrained in the gel, along with saturation index calculations, further corroborates that other than Si, the gel structure does not incorporate other major cations dissolved during leaching (Figure 1D-F). In the FA-3 ash sample, 6 M HNO<sub>3</sub> leaching extracted ~60-95% of the Fe, Ca, and Al present in the ash within the first 5 min (Figure 1D,E). Importantly, no Fe, Ca, or Al concentration decreases, indicative of product formation, were measured over time (Figure 1D). Thermodynamic calculations agree with negative saturation indices for the Fe, Ca, and Al hydroxide phases, as well as aluminosilicate clays (Figure 1F), confirming that precipitation of these phases is not favorable. In contrast, dissolved Si concentrations decrease ~10-fold as the leaching progresses from 5 min ([Si]<sub>t=5 min</sub>: ~940 ppm, Figure 1D) to 15 min ([Si]<sub>t=15 min</sub>: ~40 ppm, Figure 1D), during which time gels precipitate ubiquitously. Throughout the leaching process, the calculated saturation index of silica was positive and precipitation is expected (Figure 1F).

When 6 M leaching experiments were performed using ash feedstocks of different compositions, we noted that silica precipitation was consistently favorable, although gelation was observed only macroscopically in ashes FA-2, FA-3, and FA-4. Dissolved Si concentrations ranging between ~9 and ~85 ppm were measured in the leachates of all ash samples (Figures 2A,



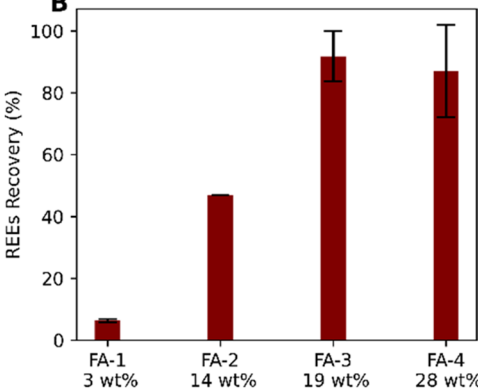


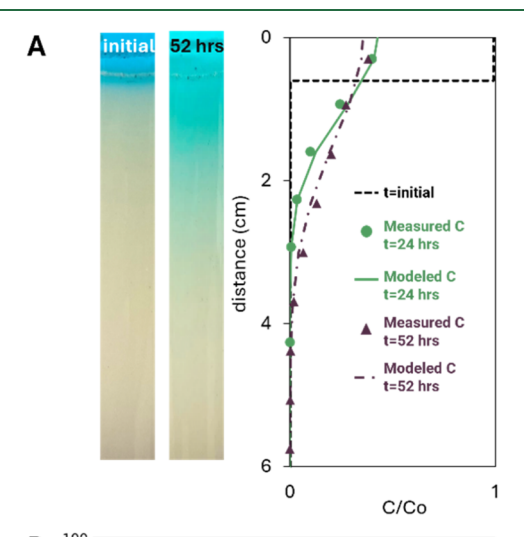
Figure 2. (A) Major cation composition data of the leachates originated from the 6 M leaching of ash samples. Initial calcium concentrations (reported here as oxide equivalent wt %) are shown below the ash sample labels and increase from left to right. For the non-log figure and the tabulated data, please refer to the SI (Figure S4, Tables S3 and S4). (B) Average REEs recovery efficiencies for each ash sample, plotted as a function of the calcium oxide concentration in the ash. Higher REEs recovery efficiencies are observed in ashes with a greater calcium oxide content.

S4, Tables S3, S4), comparable to Si solubility in concentrated HNO<sub>3</sub> solutions ([Si]  $\sim$  45 ppm). Positive saturation indices for silica in all ash leachates further corroborate their tendency to precipitate silica phases (Table S5). Kinetically favorable conditions for precipitation, however, appear to be present only in calcium-rich ashes (i.e., FA-2, FA-3, and FA-4). A first explanation for the differences in precipitation behavior is the composition of the final leachate. Specifically, metal cations in solution have been reported to accelerate silica precipitation and, therefore, ash feedstocks that release more secondary cations (i.e., major cationic species present in the ash that are not of extractive interest, including Al, Ca, Fe, Na, Mg) are expected to precipitate at faster rates than those releasing fewer cations in solution.

Another explanation for the accelerated gel formation in calcium-rich ashes is an increased level of destabilization and release of Si–O groups from the bulk ash matrix during cation exchange (i.e., M–O–Si + H<sup>+</sup>  $\rightarrow$  H–O–Si + M<sup>+</sup>). The release

of metal cations from amorphous ash matrices creates molecular interstices that enable the solid-state interdiffusion of metal cations outward and solution protons inward. <sup>12,13</sup> Si mobilization during leaching, however, can occur only after a certain degree of matrix framework destabilization during cationic exchange. Specifically, the removal of secondary cations from the ash matrix can generate Si—O tetrahedra with partial to no connectedness to the bulk matrix network, and consequently promote Si—O release into solution by reducing or eliminating the number of protonation steps needed to hydrolyze an Si—O tetrahedron. Therefore, owing to their higher cation concentrations in the ash matrices, calcium-rich samples experience more extensive cationic exchange and potentially generate larger quantities of silica that oversaturate the fluid and promote rapid gel formation.

Impact of Gels on REEs Recovery. To understand the impact of gels on REEs recovery, we evaluated the transport properties of the gel and assessed whether precipitation adversely affects REEs recovery rates (Figure 3A). Specifically, solute transport experiments were performed for Cu<sup>2+</sup> across the gels for 24 and 52 h. Here, the transport of Cu<sup>2+</sup> in the gels followed Fickian diffusion closely, where diffusion coefficients,



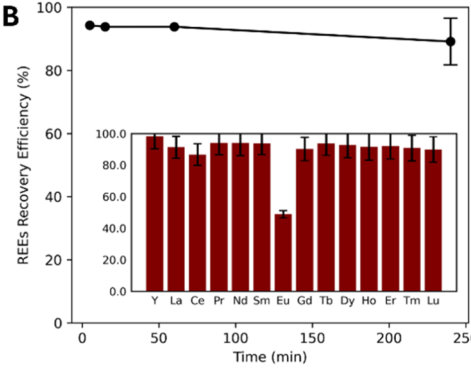


**Figure 3.** (A) Concentration profiles across the gel resulting from solute transport experiments performed for 24 and 52 h. The calculated average  $D_{\rm Cu}$  in the gelled leachate was  $\sim 5.9 \times 10^{-6}$  cm $^2/\rm s$ , which is within the same order of magnitude as  $D_{\rm Cu}$  in aqueous solution. These results suggest that the gel phase does not hinder cation transport. (B) REEs recovery over time using a 6 M HNO<sub>3</sub> leaching solution highlights that REEs extraction plateaus to  $\sim 95\%$  recovery in less than 1 h. The inset plot shows the individual REEs recovery efficiencies at 240 min.

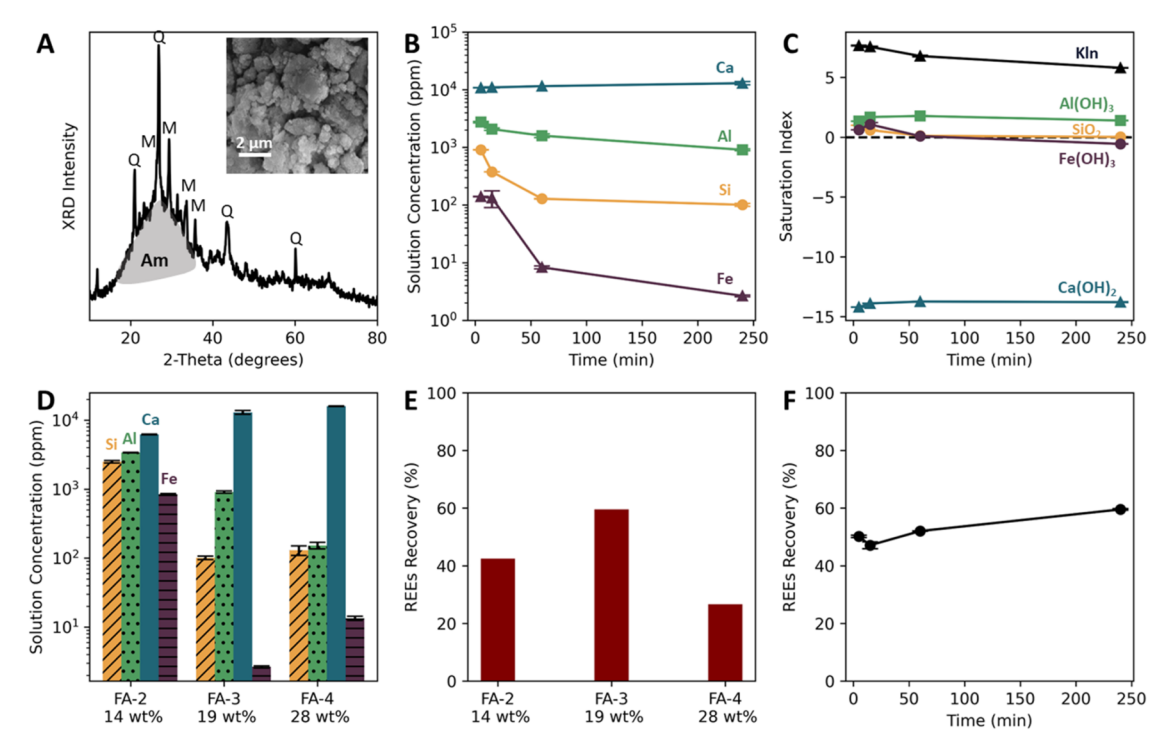


Figure 4. Characterization of flocculants formed at low molarity leaching conditions (1 M HNO<sub>3</sub>). (A) XRD data of the leaching residue, which includes both the newly formed products and remaining ash solids. The shaded gray "Am" region denotes the amorphous phase. Peaks corresponding to the unreacted quartz (Q) and mullite (M) phases present in the ash are also present. The inset image corresponds to an SEM micrograph of the flocs that precipitated during low acid concentration leaching. (B) Time-resolved fluid concentration data of major cations (Si, Ca, Al, and Fe) found in the FA-3 fly ash showing slowed reactions after  $\sim$ 1 h. (C) Saturation Indices were calculated for key phases, including amorphous silica, kaolinite, goethite, gibbsite, and portlandite. For 1 M HNO3 leaching, SI calculations suggest the thermodynamically favorable (SI > 0) precipitation of kaolinite, gibbsite (Al(OH)<sub>3</sub>), amorphous silica (SiO<sub>2</sub>), and goethite (Fe(OH)<sub>3</sub>). Recovery efficiency of major cations is not shown here since most major cations appear to precipitate. (D) Major cation concentration data for samples FA-2, FA-3, and FA-4 after a 4 h leaching period. Sample FA-1 was excluded since it yielded lower recoveries in prior experiments under high acid concentrations. Initial calcium concentrations (reported here as oxide equivalent wt. %) are shown below the ash sample labels and increase from left to right. (E) REEs recovery efficiencies for samples FA-2, FA-3, and FA-4. (F) REEs recovery efficiency for sample FA-3 during 1 M HNO<sub>3</sub> leaching, showing slowed extraction kinetics after  $\sim$  1 h.

calculated using spatially resolved  $Cu^{2+}$  concentrations in the interstitial fluids, were consistent across time ( $\sim$ 6.13  $\times$  10<sup>-6</sup> cm<sup>2</sup>/s for 24 h, and 5.69  $\times$  10<sup>-6</sup> cm<sup>2</sup>/s for 52 h).

Interestingly, the transport properties of Cu<sup>2+</sup> in the silica gels measured here are similar to values reported for Cu<sup>2+</sup> transport in aqueous solutions ((6.6 to 7.3)  $\times$  10<sup>-6</sup> cm<sup>2</sup>/s).<sup>39</sup> The gel framework, therefore, does not significantly bar the transport of cations and is not anticipated to hinder metal diffusion during acid leaching. Moreover, a comparison between the kinetics of gel formation and the kinetics of REEs recovery indicates that the accessibility of the proton to the REEs is not impacted by the gel. For sample FA-3, fluid analyses show that more than 90% of REEs are recovered within the first ~5 min of leaching, with no loss of dissolved REEs observed over extended leaching periods (i.e., no REE precipitation, Figure 3B). In contrast, complete leachate gelation requires approximately 10-15 min, suggesting that the kinetics of REEs extraction from the ash are much faster than the rate of silica transport and polymerization. REEs recovery is therefore expected to occur irrespective of gel formation based on its faster kinetics and the minimal impact of gels on cationic transport.

When compared to other gel-prone ash samples (FA-2 and FA-4, Figure 2B), we note that REEs recovery appears to follow primarily the composition of feedstock material rather than variations in gel characteristics (e.g., degree of cross-

linking, viscosity). For instance, the FA-4 ash has a higher alkali content and thus is expected to destabilize more Si–O tetrahedra during leaching and generate a more condensed (i.e., tightly packed) gel. The REEs recovery for sample FA-4, however, is equally as high as sample FA-3 (Figure 2B). Higher concentrations of major cations in solution provide further evidence of greater leaching performance of feedstocks characterized by high REEs extraction efficiency (Tables S3 and S4). Thus, although the potential impact of gel characteristics cannot be fully decoupled from the intraparticle events controlling REEs release, the results here suggest that gel condensation differences may have a limited impact on recovery.

While our results demonstrate that gelation of the leachate does not hinder REEs release from the ash particles, gel formation does have significant implications for large-scale hydrometallurgical operations. Specifically, the filterability of the leachate is compromised due to fluid retainment within the gelatinous phase, leading to leachate loss and reduced metal recovery. The gelled leachate is also a highly viscous phase that reduces mass transfer at scale, strains pumping equipment, and can create a cemented phase that clogs processing equipment. Even at low concentrations, silica gels complicate downstream processes by creating stable emulsions in solvent extraction systems that lead to reagent losses and poorer separation efficiencies. Gel formation must therefore be

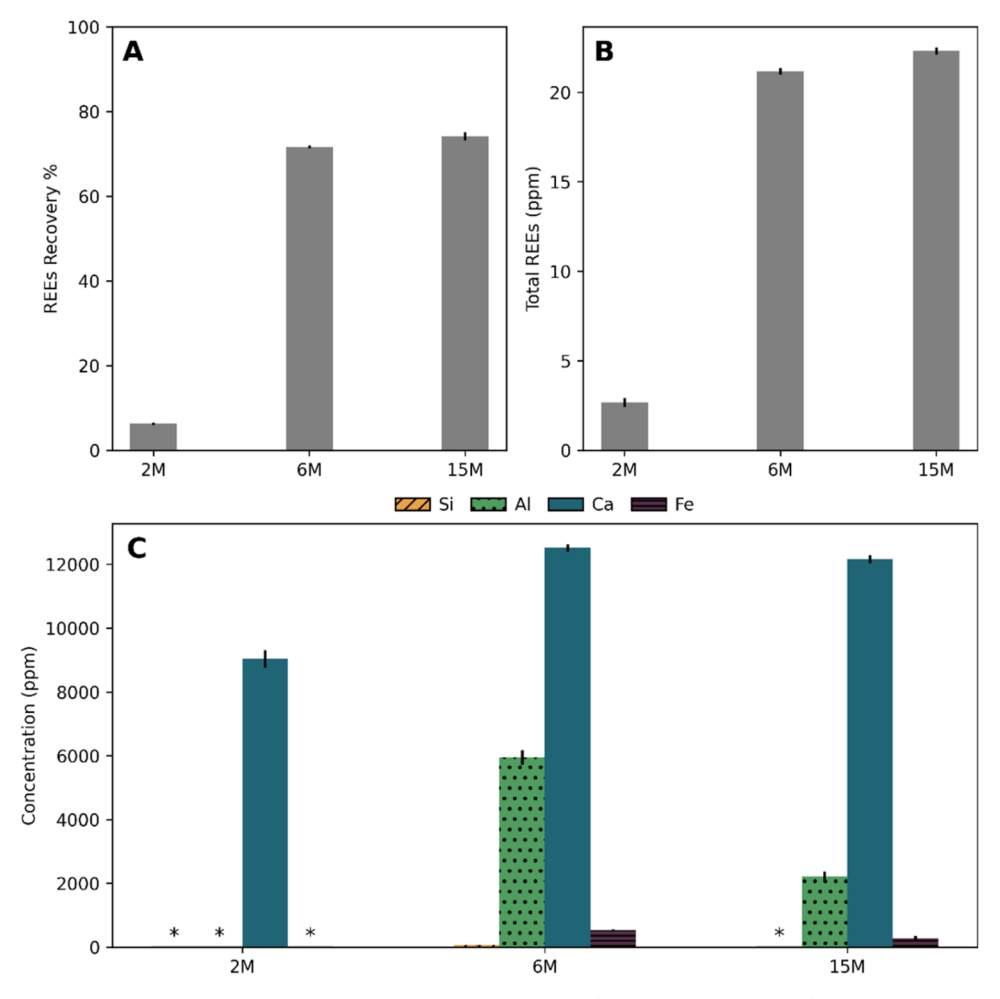


Figure 5. Acid baking experiments performed using different acid concentrations (2, 6, and 15 M HNO<sub>3</sub>) for the acid baking step, followed by water leaching. (A) REEs recovery efficiency, (B) total REEs concentration in the final leachate in ppm, and (C) concentration, in ppm, of the major cations (Si, Ca, Al, and Fe) present in the final leachate solutions. Data marked by the symbol (\*) denote that the elemental concentration was below the detection limit. For Si, this suggests concentrations below 10 ppm.

minimized to enable effective and scalable REEs extraction processes.

Low Molarity Acid Leaching. Low molarity solutions (1 and 2 M HNO<sub>3</sub>) were evaluated to minimize and, when possible, inhibit gel formation. Concentrations of 1 and 2 M HNO<sub>3</sub> were tested using an L/S ratio of 10 to evaluate REEs recovery efficiency and potential for gel mitigation.

2 M HNO<sub>3</sub> Leaching. Leaching with 2 M HNO<sub>3</sub> recovers ~ 82% of the REEs present without visible gel formation within the timeframes for leaching (~ hours), however gelation remains favorable over long periods (~ weeks). Leachate samples aged over the course of 2 weeks condensed into gelatinous phases similar to higher leaching molarity cases. Although no precipitates or gels were observed at a macroscopic scale, time-resolved fluid concentrations for 2 M leaching conditions showed a decrease in Si concentration from ~7900 ppm at 15 min to ~3800 ppm after 4 h (Figure SSA). Thermodynamic modeling indicates that the final leachate remained oversaturated with respect to silica phases ( $[Si] \sim 3800 \text{ ppm}$ ) after the 4 h leaching, and thus, further precipitation and polymerization are expected to take place. Here, Si oversaturation is enabled by the solution pH of  $\sim 1$ (Figure S6), which falls within the metastable region for Si condensation where gelation rates are minimized for pH values near or at the silica isoelectric point (pH<sub>IEP</sub>  $\sim 1$  to 3, Figure

S7).<sup>21</sup> Leaching using a 2 M HNO<sub>3</sub> solution, therefore, maintains higher concentrations of silicic acid in solution, while reducing the rate at which silicate species polymerize. Notably, while the rate of condensation (Si–O–Si formation) was reduced drastically, gelation remains favorable and progresses slowly. Therefore, the precipitation of silica species is still expected to take place, and its accumulation would present a costly challenge over longer operation periods and cycles.

1 M HNO<sub>3</sub> Leaching. Leachate gelation during REEs extraction was successfully avoided using 1 M HNO<sub>3</sub>. Floc precipitation, however, occurred for the Ca-rich ashes, and lower REEs recoveries were observed across all tested ashes (Figure 4E). For the calcium-rich FA-3 ash, low acid concentration leaching generated a precipitate that is primarily comprised of amorphous flocculants (Figure 4A). Microscopic elemental analysis using SEM-EDS of flocs from sample FA-3 shows that the main elemental composition of the formed flocculants consists primarily of Al ( $\sim$  14 wt. %), Si ( $\sim$  17 wt. %), and O ( $\sim$  45 wt. %) (Figure S8). Mineral phase characterization of the total residue (i.e., reacted ash and precipitate mixture) using XRD shows both a hump characteristic of amorphous phases as well as residual quartz and mullite phases from the residual ash (Figure 4A).

Solution pH measurements indicated a significant pH increase from an initial value of 0 to ~3.1 and ~3.3 for samples FA-3 and FA-4, respectively, within the first 5 min (Figures S9 and S10). The rapid pH rise results from the dissolution of basic compounds (calcium silicate, periclase, lime) in the calcium-rich ashes. In contrast, sample FA-2 exhibited a final leachate pH of 0.5 (Figure S9), and while the calculated saturation index indicated that the solution was oversaturated with respect to silica (Table S6), no macroscopic precipitation was observed. Time-resolved fluid concentration profiles indicate that, except for Ca, the major elements (Si, Fe, and Al) present in the FA-3 ash sample reprecipitate into flocculants. Over the course of leaching (t = 5 min to 4 h), dissolved Si and Fe concentrations decreased ~ 10-fold ([Si] ~ 910 to 100 ppm, [Fe]  $\sim$  140 to 3 ppm, Figure 4B). For Al, a 3fold concentration reduction is observed, with the concentration of Al decreasing from ~2700 ppm at 5 min to 900 ppm after 4 h (Figure 4B). Saturation index calculations corroborate that, given the final solution pH and metal concentrations in solution, the precipitation of amorphous silica, gibbsite, goethite, and clay phases is thermodynamically favorable during low molarity leaching (Figure 4C).

Leaching samples FA-3 and FA-4 using 1 M HNO<sub>3</sub> yielded REEs recovery efficiencies of only  $\sim 55$  and 27 %, respectively (Figure 4D,F). These values are significantly lower compared to those achieved with 6 M HNO3 leaching, where final extraction efficiencies of  $\sim 90$  and  $\sim 85$  % were reached for samples FA-3 and FA-4, respectively (Figure 2). REEs hydroxide formation is not thermodynamically favorable for low-acid-molarity leachates (Table S6). A possible explanation for the lower REEs recovery efficiencies is the adsorption of REEs cations onto the precipitated flocs. Experiments focused on the pH modification of ash leachates by Middleton et al. reported a decrease in REEs concentrations before reaching their solubility limit, suggesting REEs adsorption onto the precipitate phases. 16 We note, however, that stoichiometric calculations suggest that it is possible that we do not achieve full REEs recovery during 1 M HNO3 leaching owing to fewer available protons. Therefore, although adsorption is possible, acid limitations may also contribute to the decreased ultimate REEs recoveries under these conditions.

Mitigating Gel Formation: Acid Baking Followed by Water Leaching. Acid baking (120 °C, 2 h, acid molarity: 15 M) followed by water leaching, excitingly, recovered REEs with high efficacy, no visible macroscopic gels or flocs, and low final silica content in solution (Figure 5). REEs recovery efficiencies of up to ~ 74 % were achieved, with the final REEs concentration in solution of up to 24 ppm and amenable to separations downstream (Figure 5A,B). Importantly, the acid baking approach yielded lower concentrations of unsought secondary cations in the final solution and reduced the load for separation. Compared to direct leaching, the full acid strength (15 M) acid baking pretreatment reduced the concentrations of Al, Ca, and Fe in solution from 11 600 to 2200 ppm, 17 530 to 12 160 ppm, and 3500 to 280 ppm, respectively, and yielded undetectable silica concentrations in solution with no visible suspended precipitates (Figures 1D vs 5C).

These compelling results are enabled by the acid baking process, which generates an acidic environment that breaks down metal-silica bonds while limiting water availability and promoting the rapid reprecipitation of dissolved species (e.g., amorphous silica clusters, salts). Specifically, metal cations are precipitated as water-soluble salts<sup>2,3,41</sup> that are amenable to

water leaching while the silica product remains insoluble. In our coal fly ash work, the acid baking pretreatment breaks down the amorphous aluminosilicate matrix into silicic acid and soluble metals. With decreasing water concentration, amorphous insoluble Si phases and soluble metal salts precipitate. Interestingly, while high REEs recoveries found in this work suggest the formation of water—soluble REE compounds during acid baking, secondary cation concentrations in the water leachate are low (Figure 5C) and suggest the incorporation of Al, Fe, and Ca into the insoluble product. Additional studies should be performed to fully elucidate the possible phase conversions during acid baking.

To evaluate the impact of acid concentration on the effectiveness of the baking step, baking experiments were also performed using 2 and 6 M HNO<sub>3</sub> solutions. Acid baking using 2 M yielded the lowest REEs extraction efficiency, recovering only  $\sim 6$  % of the total REEs (Figure 5A). Similarly, negligible recoveries were recorded for most major cations, with the exception of Ca (Figure 5C). Acid baking experiments performed with 6 M HNO<sub>3</sub>, in contrast, yielded favorable REE extraction efficiencies of  $\sim 71$  %, equivalent to  $\sim 22$  ppm dissolved REEs in solution (Figure 5A,B). Interestingly, for effective baking conditions (i.e., 6 and 15 M solutions), we observed an inverse relationship between the acid concentration used and the purity of the final leachate. Specifically, when comparing the composition of the leachate generated following a 6 M and a 15 M baking step, we note that the Al concentration in the leachate is reduced from  $\sim 5900$  to 2200 ppm, Fe concentrations are reduced from  $\sim 530$  to  $\sim 280$ ppm, and Si concentration is reduced from 58 ppm to less than 10 ppm, respectively (Figure 5C). More concentrated acid solutions during the baking step (e.g., 15 M HNO<sub>3</sub>) therefore yielded lower concentrations of unsought secondary cations in solution. The mechanisms that lead to a decrease in the solubility of secondary cations, however, remain unclear and should be investigated further.

#### ENVIRONMENTAL IMPLICATIONS

Coal fly ash accounts for  $\sim 70$  % of solid waste generated in coal-fired power plants and poses a human health and ecological hazard to local communities and to the environment. Recently, REEs extraction has been proposed as an alternative waste management approach to traditional ash disposal. Fundamental phenomena that take place during REEs extraction from coal fly ash, however, remain poorly understood and must be further explored to ensure the scalability of this remediation-valorization method.

The work presented here advances our understanding of REEs extraction from coal fly ash by evaluating the impact of precipitate formation on the effectiveness of leach-based extractive approaches. Specifically, this study delineates the secondary phases that precipitate during acid leaching of calcium-rich fly ash, describes the implications of precipitates on the recovery of REEs, and, last, provides methods to minimize precipitates in the final leachates to enable upscaling. Under the highly acidic conditions (pH < 0) created by a 6 M HNO<sub>3</sub> leaching solution that recovers ~95% of the REEs in 1 h, silica precipitation and condensation created a gelatinous leachate. Although gels did not passivate the extraction of REEs from ash matrices, water entrainment within the gels impeded at-scale operations under these conditions. For 1 M HNO<sub>3</sub> leaching, most major elements present in calcium-rich ashes (Fe, Al, Si) were susceptible to precipitation and form

flocculants. Notably, final REEs recoveries for 1 M leaching were significantly lower, suggesting either incomplete extraction or that the flocculants adsorb some of the REEs released into the solution. Lastly, we evaluated the efficacy of acid baking followed by the water leaching approach to circumvent gel formation. Our results show that acid baking followed by water leaching enables us to achieve high REEs recovery as well as high REEs concentrations and low secondary cation concentrations in the final solution while avoiding the formation of secondary phases (e.g., gels, flocs, etc.). Overall, the findings presented here clarify the impact of key phenomena that take place during acid leaching of coal fly ash to enable the development of scalable and deployable REEs extraction processes.

# ASSOCIATED CONTENT

# **5** Supporting Information

The Supporting Information is available free of charge at https://pubs.acs.org/doi/10.1021/acs.est.5c08817.

Ash composition, including major and trace element concentrations (Tables S1 and S2); initial ash mineralogy characterized using XRD (Figure S1); calibration curve for UV-vis characterization of Cu2+ concentrations in aqueous solutions (Figure S2); SEM image and accompanying EDS spectrum of residues from 6 M HNO<sub>3</sub> leach (Figure S3); nonlog cation concentration plot and REEs recovery data for all ash samples (Figure S4); elemental concentration data for 6 M HNO<sub>3</sub> leaching experiments (Table S3). Recovery efficiency data for 6 M HNO3 leaching experiments (Table S4); concentration, elemental recovery, and saturation indices for 2 M HNO3 leaching experiments using sample FA-3 (Figure S5); temporally resolved pH data for 2 M HNO3 leaching experiment using sample FA-3 (Figure S6); silica condensation rates as a function of pH (Figure S7); saturation indices for 6 and 1 M HNO<sub>3</sub> leaching experiments (Tables S5 and S6); SEM image and accompanying EDS spectrum of residues from 1 M HNO<sub>3</sub> leach (Figure S8); pH data for various ashes during leaching experiments (Figures S9 and S10) (PDF)

# AUTHOR INFORMATION

#### **Corresponding Author**

Wen Song — Center for Subsurface Energy and the Environment, The University of Texas at Austin, Austin, Texas 78712, United States; Texas Materials Institute, The University of Texas at Austin, Austin, Texas 78712, United States; orcid.org/0000-0003-1913-4503; Phone: (512) 471-5789; Email: wensong@utexas.edu

#### Author

Sheila Gerardo – Center for Subsurface Energy and the Environment, The University of Texas at Austin, Austin, Texas 78712, United States

Complete contact information is available at: https://pubs.acs.org/10.1021/acs.est.5c08817

## Notes

The authors declare no competing financial interest.

#### ACKNOWLEDGMENTS

This material is based upon work supported by the National Science Foundation under Grant No. 2145374.

#### REFERENCES

- (1) Balaram, V. Rare earth elements: A review of applications, occurrence, exploration, analysis, recycling, and environmental impact. *Geosci. Front.* **2019**, *10*, 1285–1303.
- (2) Vidal, O.; Goffé, B.; Arndt, N. Metals for a Low-Carbon Society. *Nat. Geosci.* **2013**, *6*, 896.
- (3) Alonso, E.; Sherman, A. M.; Wallington, T. J.; et al. Evaluating rare earth element availability: A case with revolutionary demand from clean technologies. *Environ. Sci. Technol.* **2012**, *46*, 3406–3414.
- (4) Dutta, T.; Kim, K. H.; Uchimiya, M.; et al. Global demand for rare earth resources and strategies for green mining. *Environ. Res.* **2016**, *150*, 182–190.
- (5) Imholte, D. D.; Nguyen, R.; Vedantam, A.; et al. An assessment of U.S. rare earth availability for supporting U.S. wind energy growth targets. *Energy Policy* **2018**, *113*, 294–305.
- (6) International Energy Agency (IEA). The Role of Critical World Energy Outlook Special Report Minerals in Clean Energy Transitions. 2022.
- (7) Mardon, S. M.; Hower, J. C. Impact of Coal Properties on Coal Combustion By-Product Quality: Examples from a Kentucky Power Plant. *Int. J. Coal Geol.* **2004**, *59*, 153–169.
- (8) Seredin, V. V.; Dai, S. Coal Deposits as Potential Alternative Sources for Lanthanides and Yttrium. *Int. J. Coal Geol.* **2012**, *94*, *67*–93.
- (9) Taggart, R. K.; Hower, J. C.; Dwyer, G. S.; Hsu-Kim, H. Trends in the Rare Earth Element Content of U.S.-Based Coal Combustion Fly Ashes. *Environ. Sci. Technol.* **2016**, *50*, 5919—5926.
- (10) Scott, C.; Kolker, A.FS 2019-3048: Rare Earth Elements in Coal and Coal Fly Ash USGS Fact Sheet 2019, p 3048.
- (11) U.S. Geological Survey. Mineral Commodity Summaries 2024; Vol. 2024.
- (12) Gerardo, S.; Davletshin, A. R.; Loewy, S. L.; Song, W. From Ashes to Riches: Microscale Phenomena Controlling Rare Earths Recovery from Coal Fly Ash. *Environ. Sci. Technol.* **2022**, *56*, 16200–16208
- (13) Gerardo, S.; Matthews, K.; Warner, J.; Song, W. Role of Nanoscale Crystallinity on the Recovery of Rare Earth Elements (REEs) from Coal Fly Ash. *Environ. Sci. Technol. Lett.* **2023**, *10*, 943–
- (14) Dai, S.; Finkelman, R. B.; French, D.; et al. Modes of occurrence of elements in coal: A critical evaluation. *Earth-Sci. Rev.* **2021**, 222, 103815.
- (15) Thomas, B. S.; Dimitriadis, P.; Kundu, C.; et al. Extraction and separation of rare earth elements from coal and coal fly ash: A review on fundamental understanding and on-going engineering advancements. J. Environ. Chem. Eng. 2024, 12, 112769.
- (16) Middleton, A.; Park, D. M.; Jiao, Y.; Hsu-Kim, H. Major element composition controls rare earth element solubility during leaching of coal fly ash and coal by-products. *Int. J. Coal Geol.* **2020**, 227, 103532 DOI: 10.1016/j.coal.2020.103532.
- (17) Suraneni, P.; Burris, L.; Shearer, C. R.; Hooton, R. D. ASTM C618 Fly Ash Specification: Comparison with Other Specifications, Shortcomings, and Solutions. *ACI Mater.* **2021**, *118*, 157–167.
- (18) King, J. F.; Taggart, R. K.; Smith, R. C.; Hower, J. C.; Hsu-Kim, H. Aqueous acid and alkaline extraction of rare earth elements from coal combustion ash. *Int. J. Coal Geol.* **2018**, *195*, 75–83.
- (19) Liu, P.; Huang, R.; Tang, Y. Comprehensive Understandings of Rare Earth Element (REE) Speciation in Coal Fly Ashes and Implication for REE Extractability. *Environ. Sci. Technol.* **2019**, *53*, 5369–5377.
- (20) Stoy, L.; Diaz, V.; Huang, C. H. Preferential Recovery of Rare-Earth Elements from Coal Fly Ash Using a Recyclable Ionic Liquid. *Environ. Sci. Technol.* **2021**, *55*, 9209–9220.

- (21) Queneau, P. B.; Berthole, C. E. Silica in hydrometallurgy: An overview. *Can. Metall. Q.* **1986**, 25, 201–209.
- (22) Demol, J.; Ho, E.; Soldenhoff, K.; Senanayake, G. The sulfuric acid bake and leach route for processing of rare earth ores and concentrates: A review. *Hydrometallurgy* **2019**, *188*, 123–139.
- (23) Davris, P.; Stopic, S.; Balomenos, E.; et al. Leaching of rare earth elements from eudialyte concentrate by suppressing silica gel formation. *Miner. Eng.* **2017**, *108*, 115–122.
- (24) Rivera, R. M.; Ulenaers, B.; Ounoughene, G.; Binnemans, K.; Van Gerven, T. Extraction of rare earths from bauxite residue (red mud) by dry digestion followed by water leaching. *Miner. Eng.* **2018**, 119, 82–92.
- (25) Nawab, A.; Yang, X.; Honaker, R. Parametric study of an acid baking process for rare earth element recovery from a bituminous-coal source. *Int. J. Coal Prep. Util.* **2024**, 44 (8), 1130–1154, DOI: 10.1080/19392699.2023.2269094.
- (26) Nawab, A.; Yang, X.; Honaker, R. An acid baking approach to enhance heavy rare earth recovery from bituminous coal-based sources. *Miner. Eng.* **2022**, *184*, No. 107610.
- (27) Martell, A. E.; Smith, R. M. Critical Stability Constants: Inorganic Complexes 2004; Vol. 4.
- (28) Shiery, R. C.; Fulton, J. L.; Balasubramanian, M.; et al. Coordination Sphere of Lanthanide Aqua Ions Resolved with Ab Initio Molecular Dynamics and X-ray Absorption Spectroscopy. *Inorg. Chem.* **2021**, *60*, 3117–3130.
- (29) Diakonov, I. I.; Tagirov, B. R.; Ragnarsdottir, K. V. Standard Thermodynamic Properties and Heat Capacity Equations for Rare Earth Element Hydroxides: I. La(OH)3(s) and Nd(OH)3(s). Comparison of Thermochemical and Solubility Data. *Radiochim. Acta* 1998, 81, 107–116.
- (30) Pelletier, M. J. Quantitative analysis using Raman spectrometry. *Appl. Spectrosc.* **2003**, *57*, 20A-42A, DOI: 10.1366/000370203321165133.
- (31) Geisler, T.; Dohmen, L.; Lenting, C.; Fritzsche, M. B. K. Realtime in situ observations of reaction and transport phenomena during silicate glass corrosion by fluid-cell Raman spectroscopy. *Nat. Mater.* **2019**, *18*, 342–348.
- (32) Lenting, C.; Geisler, T. Corrosion of ternary borosilicate glass in acidic solution studied in operando by fluid-cell Raman spectroscopy. *NPJ Mater. Degrad.* **2021**, *5*, 37 DOI: 10.1038/s41529-021-00182-5.
- (33) Chancey, R. T.; Stutzman, P.; Juenger, M. C. G.; Fowler, D. W. Comprehensive phase characterization of crystalline and amorphous phases of a Class F fly ash. *Cem. Concr. Res.* **2010**, *40*, 146–156.
- (34) Iler, R. The Chemistry of Silica Solubility, Polymerization, Colloid and Surface Properties, and Biochemistry 1979.
- (35) Lazaro, A.; Vilanova, N.; Barreto Torres, L. D.; et al. Synthesis, Polymerization, and Assembly of Nanosilica Particles below the Isoelectric Point. *Langmuir* **2017**, *33*, 14618–14626.
- (36) Elmer, T. H.; Nordberg, M. Solubility of Silica in Nitric Acid Solutions. *J. Am. Ceram. Soc.* **1958**, *41*, 517–520.
- (37) Gorrepati, E. A.; Wongthahan, P.; Raha, S.; Fogler, H. S. Silica precipitation in acidic solutions: Mechanism, pH effect, and salt effect. *Langmuir* **2010**, *26*, 10467–10474.
- (38) Brantley, S. L.; Kubicki, J. D.; White, A. F. Kinetics of Water-Rock Interaction; Springer, 2008.
- (39) Emanuel, A.; Olander, D. R. Diffusion Coefficients of Copper Sulfate in Water and Water in N-Butyl Alcohol. https://pubs.acs.org/sharingguidelines.
- (40) Abkhoshk, E.; Jorjani, E.; Al-Harahsheh, M. S.; Rashchi, F.; Naazeri, M. Review of the hydrometallurgical processing of nonsulfide zinc ores. *Hydrometallurgy* **2014**, *149*, 153–167.
- (41) Voßenkaul, D.; Birich, A.; Müller, N.; Stoltz, N.; Friedrich, B. Hydrometallurgical Processing of Eudialyte Bearing Concentrates to Recover Rare Earth Elements Via Low-Temperature Dry Digestion to Prevent the Silica Gel Formation. *J. Sustainable Metall.* **2017**, *3*, 79–89.

- (42) Vaccarezza, V.; Anderson, C.Beneficiation and Leaching Study of Norra Kärr Eudialyte Mineral. In *TMS Annual Meeting and Exhibition*; Springer: Cham, 2018; pp 39–51.
- (43) Chen, Y.; Fan, Y.; Huang, Y.; et al. A comprehensive review of toxicity of coal fly ash and its leachate in the ecosystem. *Ecotoxicol. Environ. Saf.* **2024**, *269*, No. 115905.
- (44) Wu, J.; Tou, F.; Yang, Y.; et al. Metal-Containing Nanoparticles in Low-Rank Coal-Derived Fly Ash from China: Characterization and Implications toward Human Lung Toxicity. *Environ. Sci. Technol.* **2021**, *55*, 6654.



CAS BIOFINDER DISCOVERY PLATFORM™

# CAS BIOFINDER HELPS YOU FIND YOUR NEXT BREAKTHROUGH FASTER

Navigate pathways, targets, and diseases with precision

**Explore CAS BioFinder** 

